THE UNIVERSITY OF CHICAGO

LONG-TIME EVOLUTION OF INTERFACIAL STRUCTURE OF PARTIAL WETTING

A DISSERTATION SUBMITTED TO
THE FACULTY OF THE DIVISION OF THE PHYSICAL SCIENCES
IN CANDIDACY FOR THE DEGREE OF
DOCTOR OF PHILOSOPHY

DEPARTMENT OF PHYSICS

BY
MENGFEI HE

CHICAGO, ILLINOIS
DECEMBER 2019

An experiment is not simply shown because it is beautiful, but their chief object is to enable you to see for yourselves what the true answers are to questions that I shall ask.

- Sir Charles Vernon Boys, F.R.S., 1889

TABLE OF CONTENTS

LIST OF FIGURES

ACKNOWLEDGMENTS

I am deeply indebted to Sidney Nagel for his advising and mentoring. He has inspired me of how to carry out experiments with passion, care and taste. I thank Anthony LaTorre for extensive discussions on various computational techniques. I also thank Amy Schulz for kindly coordinating a financial support.

This work was primarily supported by the University of Chicago MRSEC, funded by the National Science Foundation under Grant No. DMR-1420709 and by NSF Grant No. DMR-1404841.

ABSTRACT

When a solid plate is withdrawn from a partially wetting liquid, a liquid layer dewets the moving substrate. High-speed imaging reveals alternating thin and thick regions in the entrained layer in the transverse direction at steady state. This paper systematically compares this situation to the reversed process, forced wetting, where a solid entrains an air layer along its surface as it is pushed into a liquid. To quantify the absolute thickness of these steady-state structures precisely, I have developed an optical technique, taking advantage of the angle dependence of interference, combined with a method based on a maximum likelihood estimation. The data show that the thicknesses of both regions of the film scale with the capillary number, Ca. In addition, a new region is observed during onset which differs from the behavior predicted by previous models.

CHAPTER 1

INTRODUCTION

When a solid is rapidly withdrawn from a liquid bath, a film of liquid is dragged along the solid surface. This film dewets the surface as it is dragged down by gravity. Conversely, when rapidly pushed into a liquid bath, the solid entrains a film of surrounding air along its surface. This is commonly known as "forced wetting". This paper will show that forced wetting and dewetting share many similarities.

The phenomenon of forced wetting or dewetting occurs in many daily processes. Typically, it is not possible to see the steady-state behavior of such processes. The duration of the event is too short and the geometry of the substrate is too irregular. However, a controlled experiment can be prolonged to reveal a stationary wetting/dewetting layer that can be quantified with high-speed video techniques. In our previous study [7] of forced wetting, the air layer entrained by a long ribbon of mylar tape pushed into a liquid bath develops prominent and surprising structures. Figure 1.1a shows that at steady state, the air layer assumes a V shape with two extremely flat and thin sections positioned at the upper corners.

This paper extends this study to the process of dewetting. Figure 1.1b shows that at steady state, the entrained liquid layer forms an upside-down V shape. Both in the case of wetting and dewetting, it was shown [7], that inside a triangular-shaped contact line, two sharply different thicknesses stably coexist. There is a thin-thick alternation of the entrained liquid that appears near the bottom (in dewetting) or near the top (in the case of wetting) across the width of the substrate. There is a striking similarity between the structures found in both experiments.

Extensive studies have been dedicated to the contact-line dynamics and layer thickness at the *onset* of the entrainment during dewetting (e.g., [15, 2, 16]). By studying the contact line after it has evolved to its steady state, the prominent structure in the entrained liquid layer can be measured. This paper reports measurements of the local contact-line motion at both onset and in steady state. In addition, by measuring interference fringes as a function

of the angle of incidence, the *absolute* thickness of the wetting layer was determined as a function of different control parameters.

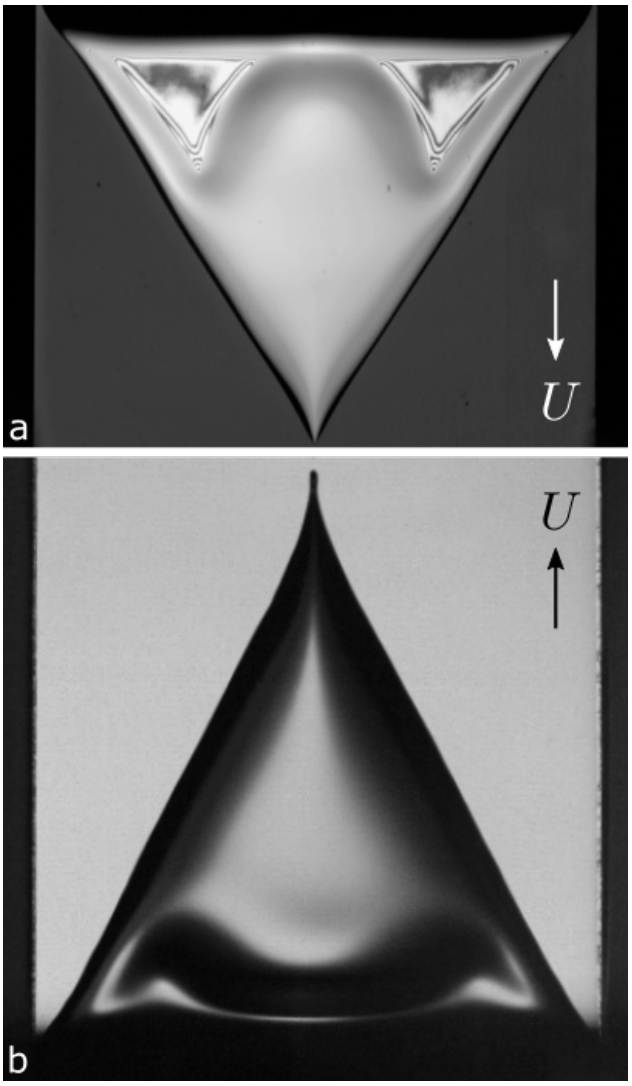

Figure 1.1: (a) Steady state of an entrained air film in forced wetting. A mylar tape of width $w = 12.7$ mm plunges vertically into a water-glycerin mixture of viscosity $\eta = 226$ cP at $U = 130$ mm/s. The entrained air layer assumes a V shape with two thin, flat sections at the upper corners. (b) Steady state of a liquid film in dewetting. An acrylic plate of width $w = 20.3$ mm is pulled vertically out of a water-glycerin bath of viscosity $\eta = 107$ cP at $U = 4.4$ mm/s. An entrained liquid layer forms an upside-down V shape with two thin sections at the lower corners.

CHAPTER 2

METHODS

2.1 Mechanical apparatus and fluids used

For the dewetting experiments, the solid substrate was installed on a vertical linear guide (PBC Linear ^{TM}, IVTAAW) to ensure smooth vertical motion. The stage of the linear guide system was attached to a roller chain, driven by a Silverpak 17 integrated step motor (NEMA 17). The velocity of the substrate ranged from 1 mm/s to 400 mm/s with <5% fluctuation for each velocity. Water-glycerin mixtures were used as the viscous liquid. In different experiments, different viscosities, 0.9 cP $\leq \eta \leq$ 1264 cP, were used. The viscosity was measured by an Anton Paar MCR301 rheometer or by manual glass viscometers (CANNON-Ubbelohde). The liquid density ρ and interfacial tension γ were measured by a KRÜSS tensiometer; the measured values were consistent with values from literature [17, 18]. Measurement of refractive index (consistent with literature [8]) and thickness of the entrained liquid layer are described below.

2.2 Substrate preparation

In the dewetting experiments, the solid substrate consists of slender rectangular sections (560 mm×3.2 mm) of black cast acrylic, cut to various widths, w = 12.3, 17.1, 24.9, 35.3, 50.5 mm. The edges were further milled and polished to prevent contact-line pinning during the experiments. The substrate surface was first wiped with Isopropyl alcohol to remove chemical residues from the manufacturing process. Rain-X® Original Glass Water Repellent (PDMS) was then applied to the surface and then wiped off. A droplet of water-glycerin mixture makes a static contact angle of 63° (receding) to 74°(advancing) with the prepared surface. For the forced-wetting experiments, commercial magnetic mylar tape (cassette tape with w = 6.4 mm, VHS tape with w = 12.7 mm and recording tape with w = 25.4 mm) was

used as the substrate.

2.3 Measurement of absolute thickness: principle

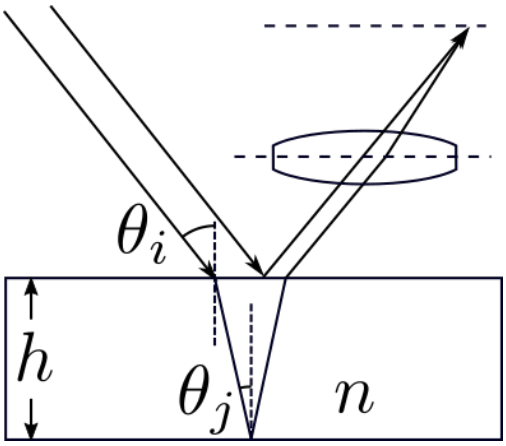

Figure 2.1: Schematic of interference produced by a beam with angle of incidence θ_i onto a sample of thickness h. Light reflected from top surface at θ_i and bottom surface at θ_j interfere at the focal plane of a lens placed above.

When a parallel beam of light is incident upon a transparent sample of thickness h with an angle of incidence θ_i, the reflected beam from the top surface at angle θ_i and the one from the bottom surface at θ_j are brought together by a lens placed above, as shown in Fig. 2.1. Interference occurs at the focal plane of the lens. Considering the phase change upon reflection, the optical path difference is $2nh\cos\theta_j + \lambda/2$, where n is the refractive index of the sample and λ is the wavelength of the light source. The intensity of interference depends on the angle of incidence θ_i. When the interference is completely destructive:

$$2nh\cos\theta_j = m\lambda, \tag{2.1}$$

where m is an integer indicating the order of the destructive interference. All the rays that produce a single dark fringe correspond to the same value of θ_j. These fringes are fringes of equal inclination. When the angle of incidence is changed from θ_{i1} to θ_{i2} such that the order

of interference increases by $\Delta m = 1$, from Eq. 2.1 the corresponding θ_{j1} and θ_{j2} satisfy:

$$2nh(\cos\theta_{j2} - \cos\theta_{j1}) = \lambda.$$

Since θ_j is related to θ_i through Snell's law:

$$\sin\theta_i = n\sin\theta_j, \tag{2.2}$$

we have

$$2nh(\cos\arcsin\frac{\sin\theta_{i2}}{n} - \cos\arcsin\frac{\sin\theta_{i1}}{n}) = \lambda. \tag{2.3}$$

If θ_{i1} and θ_{i2} can be measured, Eq. 2.3 gives a one-to-one relation between h and n. If such measurements are performed for two thicknesses, h_a and h_b, with a known difference:

$$h_a - h_b = \delta h, \tag{2.4}$$

then n, h_a and h_b can be uniquely identified from Eq. 2.3 and Eq. 2.4. In particular, if n is known beforehand or can be calibrated using Eq. 2.3 for a known h, then h of the sample can be directly deduced from Eq. 2.3 alone. Notice that no small-angle approximation has been assumed, making the above analysis valid for arbitrary angles of incidence.

2.4 Measurement of absolute thickness: setup

The top view of the experimental setup is shown in Fig. 2.2. The setup design is similar to that of [6]. The solid substrate (①) is continuously raised out of a tank (②) of liquid, entraining a layer (③) along its surface. A convex lens (Nikon f=50mm, 1:1.8) is used to focus a parallel beam of light onto the surface of the liquid layer. A wide spread of angles of incidence can thus be obtained at a single spot of the sample. Because of the axial

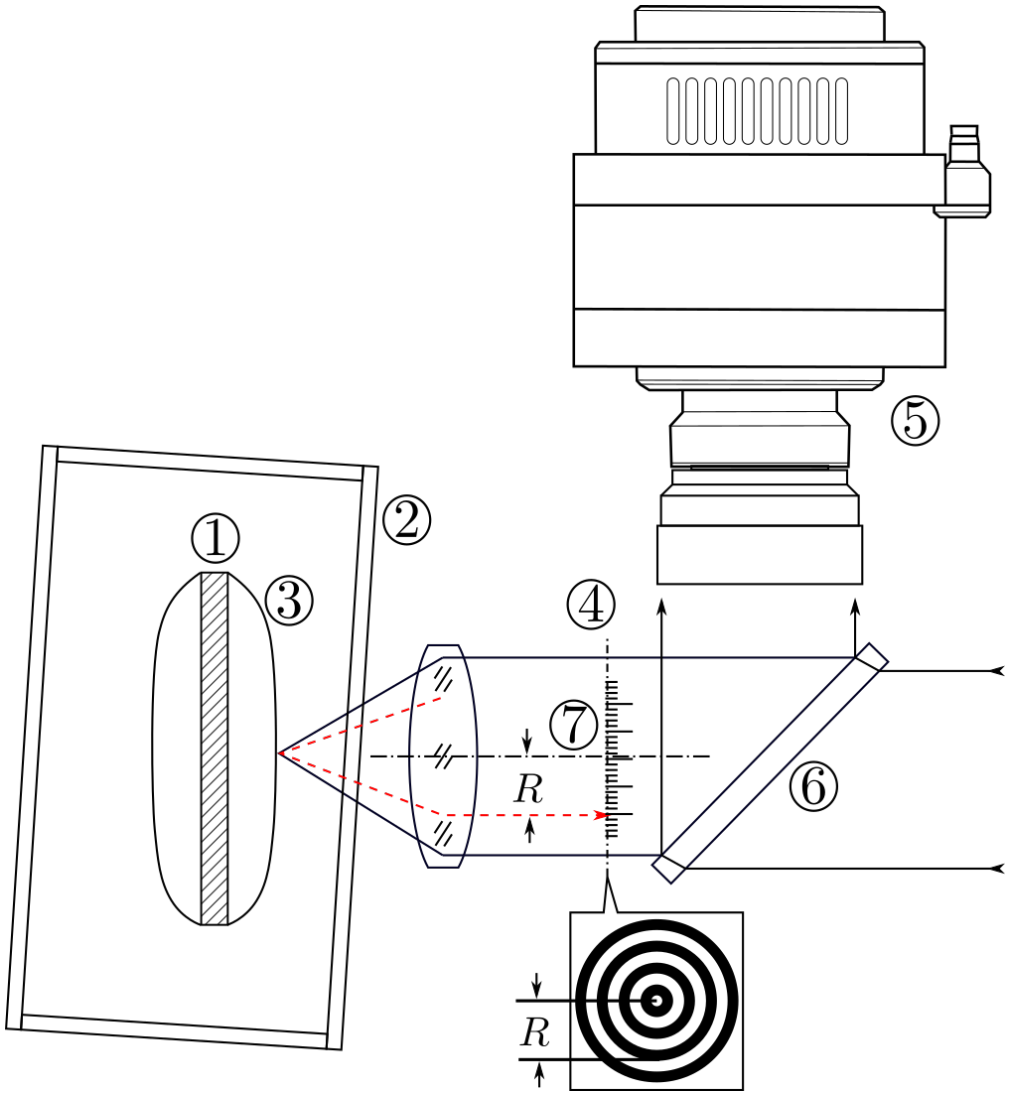

Figure 2.2: Top view of the experimental setup for measuring the absolute thickness of the entrained layer.
①: moving substrate (toward the reader);
②: tank containing a liquid bath;
③: entrained layer of fluid;
④: focal plane of a lens placed in front of ②;
⑤: high-speed camera;
⑥: half-silvered mirror;
⑦: transparent reticle.

symmetry of the lens system, the reflected light makes concentric dark fringes (fringes of equal inclination), projected by the lens onto its focal plane on the other side (④). A high-speed (Phantom®) camera (⑤) is focused on the same plane (④) to record the interference fringes through a half-silvered mirror (⑥). A reticle (⑦) is also placed in the parallel beam in order to set the measurement scale. The tank (②) is slightly tilted so that reflections from the front wall do not interfere with the light reflecting from the liquid. Tracing the ray (red, dashed line) for a specific angle of incidence θ_i shows that the corresponding radius of fringe R satisfies:

$$\sin\theta_i = \frac{R}{\sqrt{R^2+f^2}}, \tag{2.5}$$

where f is the focal length of the lens. Eq. 2.5 shows that measuring the fringe radius R, determines the angle of incidence θ_i. From Eq. 2.3, radii R_{1a} and R_{2a} of adjacent fringes of frame a of the high-speed video gives:

$$2nh_a(\cos\arcsin\frac{\frac{R_{2a}}{\sqrt{R_{2a}^2+f^2}}}{n} - \cos\arcsin\frac{\frac{R_{1a}}{\sqrt{R_{1a}^2+f^2}}}{n}) = \lambda. \tag{2.6a}$$

Similarly, for frame b:

$$2nh_b(\cos\arcsin\frac{\frac{R_{2b}}{\sqrt{R_{2b}^2+f^2}}}{n} - \cos\arcsin\frac{\frac{R_{1b}}{\sqrt{R_{1b}^2+f^2}}}{n}) = \lambda. \tag{2.6b}$$

Fluctuation of the sample thickness h makes the concentric fringe pattern shrink (if h increases) or grow (if h decreases). The thickness difference between frames a and b can be calculated by keeping track of the number p of rings that appear or disappear into the

central spot between the two frames:

$$h_a - h_b = \frac{p\lambda}{2n} \tag{2.7}$$

By root finding equations of Eqs. 2.6a, 2.6b and 2.7 numerically, the values of n, h_a and h_b can be uniquely identified. A synchronized high-speed camera (not shown), placed at an oblique angle in front of the tank, produces an image of the spot where the measurement is carried out.

CHAPTER 3

DATA FITTING: LIKELIHOOD MAXIMIZATION

In thickness measurements, one needs to convert data images of interference fringes to thickness information. It can be extremely difficult to extract fringe patterns from noisy data images. Local edge detection algorithms often perform poorly for patterns whose length scales span multiple orders of magnitude in the presence of a wide range of noise and artifacts (*e.g.*, shadows, lens flares, etc.). An example is shown in the third frame of Fig. 4.11a.

Since the physical model, *i.e.*, the relation between fringe configuration and thickness h, is known, I approach this problem using likelihood maximization. For a data image the measured pixel intensity of coordinate (x, y) is $X(x, y)$. The parameters of the model are denoted as β, the log-probability $\log P$ for all pixels of the data image taking the current values is:

$$\begin{aligned} \log P &= \log \prod_{x,y} P(X(x,y), \beta) \\ &= \log \prod_{x,y} P(X(x,y)|\beta) P(\beta) \\ &\propto \sum_{x,y} \log P(X(x,y)|\beta). \end{aligned} \tag{3.1}$$

In the last step above, $P(\beta)$ is omitted since the model parameter vector β is not a random vector. The best β that fits the data is that which maximizes the log-likelihood $l(\beta) \equiv \sum_{x,y} \log P(X(x,y)|\beta)$ (viewed as a function of β):

$$\beta_{\text{optimal}} = \underset{\beta}{\operatorname{argmax}}\, l(\beta). \tag{3.2}$$

The expression of $l(\beta)$ depends on how the pixel fluctuation is modelled. Consider the simple case of normal distribution $P(X(x,y)|\beta) \propto \exp[-(X(x,y) - X_0(x,y,\beta))^2/\sigma^2]$ where $X_0(x, y, \beta)$ is the expected pixel intensity from the physical model given a particular vector

β. Then we have:

$$l(\beta) \propto \sum_{x,y} -(X(x,y) - X_0(x,y,\beta))^2. \tag{3.3}$$

Thus, from Eq. 3.2

$$\beta_{\text{optimal}} = \underset{\beta}{\text{argmin}} \sum_{x,y} (X(x,y) - X_0(x,y,\beta))^2. \tag{3.4}$$

Therefore, under the assumption of normal distribution of pixel intensity, finding the optimal parameter β amounts to a least-square regression.

In the case of dewetting, the interference fringes are concentric circles centered at (x_c, y_c). We take h, x_c and y_c as 3 fitting parameters. Combining Eq. 2.1, Eq. 2.2 and Eq. 2.5, the expected intensity $X_0(x,y,\beta))$ is given by:

$$\begin{cases} X_0(x,y,\beta)) = \dfrac{1}{2} + \dfrac{1}{2}\cos(\dfrac{2\pi}{\lambda} 2nh\cos\theta_j + \pi) \\ \sin\theta_j = \dfrac{1}{n}\sqrt{\dfrac{(x-x_c)^2 + (y-y_c)^2}{(x-x_c)^2 + (y-y_c)^2 + f^2}} \\ \beta = (h, x_c, y_c). \end{cases} \tag{3.5}$$

Substituting Eq. 3.5 into Eq. 3.4 gives the expression

$$\beta_{\text{optimal}} = (h_{\text{optimal}}, x_{c,\text{optimal}}, y_{c,\text{optimal}}). \tag{3.6}$$

Since the right-hand-side of Eq. 3.4 is highly non-convex, β_{optimal} is found by brute-force searching through all nodes in (h, x_c, y_c) parameter space, with step resolution $\delta h = \lambda/(4n)$, $\delta x_c = \delta y_c = 1$pixel. If the refractive index n is not known beforehand, we can use the same idea of comparing two frames of thickness difference $h_a - h_b = p\lambda/2n$ with known centers $(x_{c,a}, y_{c,a})$ and $(x_{c,b}, y_{c,b})$. An exhaustive search in the parameter space $\beta = (h, h + p\lambda/2n, n)$ to maximize the joint likelihood of the two frames (summation over all pixels for two frames

in Eq. 3.4) gives the optimal n.

Similarly for the case of forced wetting, I use normal incidence only and model the interference fringes of equal height. We divide the patterned area into smaller parts, whose thickness can be approximated by a quadratic expansion. This is shown in Eq. 3.7. Since there are 6 components to optimize in β of this model, I use a basin-hopping minimizing algorithm instead of brute-force searching.

$$\begin{cases} X_0(x,y,\beta)) = \frac{1}{2} + \frac{1}{2}\cos(\frac{2\pi}{\lambda}2nh(x,y,\beta) + \pi) \\ h(x,y,\beta) = \beta_1 x^2 + \beta_2 y^2 + \beta_3 xy \\ \qquad\qquad + \beta_4 x + \beta_5 y \\ \qquad\qquad + \beta_6 \\ \beta = (\beta_1, \beta_2, \beta_3, \beta_4, \beta_5, \beta_6). \end{cases} \tag{3.7}$$

CHAPTER 4

RESULT

4.1 Formation of a V shape

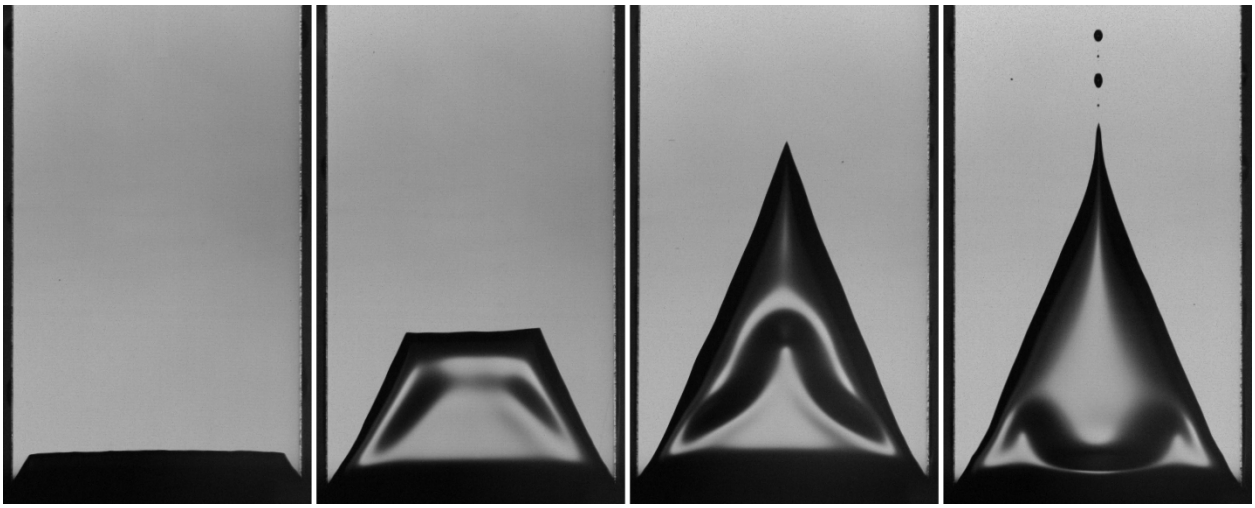

Figure 4.1: Images of a typical evolution of a dewetting liquid layer, for a duration ≈ 30 s. An acrylic plate of width, $w = 20.3$ mm, is pulled vertically out of a water-glycerin bath of viscosity $\eta = 107$ cP at $U = 4.4$ mm/s. The fluid layer reaches its steady state in the last frame. (The images are not evenly spaced in time in order to show the different stages clearly.)

Figure 4.1 shows a series of images of a fluid being pulled out of a bath by a flat substrate with straight edges. The substrate travels vertically upward at a constant velocity while the liquid forms a thin layer entrained to its surface. The contact line is where the liquid, air and solid meet. Initially, as shown in the first frame, the contact line rises from the bath in the form of a trapezoid composed of a central nearly horizontal section with two short sloping sides. In the second frame, the trapezoid grows in height. The sides remain at the same angle and the central horizontal section advances upward and becomes narrower. Just behind the contact line there is a thick rim; further back there is an extended thin, flat region. In the third frame the horizontal contact line moves upward until the trapezoid closes into a triangle. At this point, the central part of the thick rim starts to widen and

spread downward. In the final frame, as the system reaches its steady-state shape, the thin part is split into two smaller sections at the lower corners of the entrained fluid.

There appears a thin-thick alternation in the spanwise direction near the bottom of the entrained layer. When the velocity of the substrate is large enough, small liquid drops, attached to the moving substrate, emerge at the tip of the triangular pocket as shown in the last frame.

The number of alternating undulations of the layer thickness in the transverse direction depends on the width of the substrate. Figure 4.2a shows the steady state of forced wetting on mylar surface of width $w = 25.4$mm. Compared to Fig. 1.1a (substrate width $w = 12.7$ mm), Fig. 4.2a shows that near the top of the V there are 4 thin sections. The thin-thick features are more extended for wider substrates than they are for a narrower ones.

The same trend applies for the case of dewetting. Fig. 4.2b shows the dewetting film contains multiple marked thin-thick alternations for a $w = 35.3$ mm wide acrylic plate.

To quantify this trend, I measured in dewetting the width of the thick bulge as indicated by the dashed line in Fig. 4.2b. Fig. 4.3a shows that this width does not remain a constant with increasing substrate width. For wide substrates, $w > 70$ mm in the case of water dewetting on mylar, the adjacent thick parts constantly merge and re-split, so the width of a single bulge fluctuates considerably. Despite these fluctuations, Fig. 4.3b shows that there is linear relationship between the number of thick bulges versus the substrate width, w.

The lateral shape of the thick bulges in forced wetting, on the other hand, is very well defined. A large portion near the tip of the thick section can be approximated by a circle, as indicated in Fig. 4.2b. In Fig. 4.4 I have plotted the measured radius, R, of the fitted circle, versus liquid viscosity η, for a fixed substrate width $w = 12.7$ mm. The error bars indicate the influence on R of different substrate velocities. The radius decreases with an increase of the liquid viscosity, and saturates at a value close to the capillary length $l = \sqrt{\gamma/\Delta\rho g}$, independent of the substrate velocity. This suggests that at a large viscosity (> 90cP) the lateral shape of the thin-thick boundary of the air layer is selected by a balance between

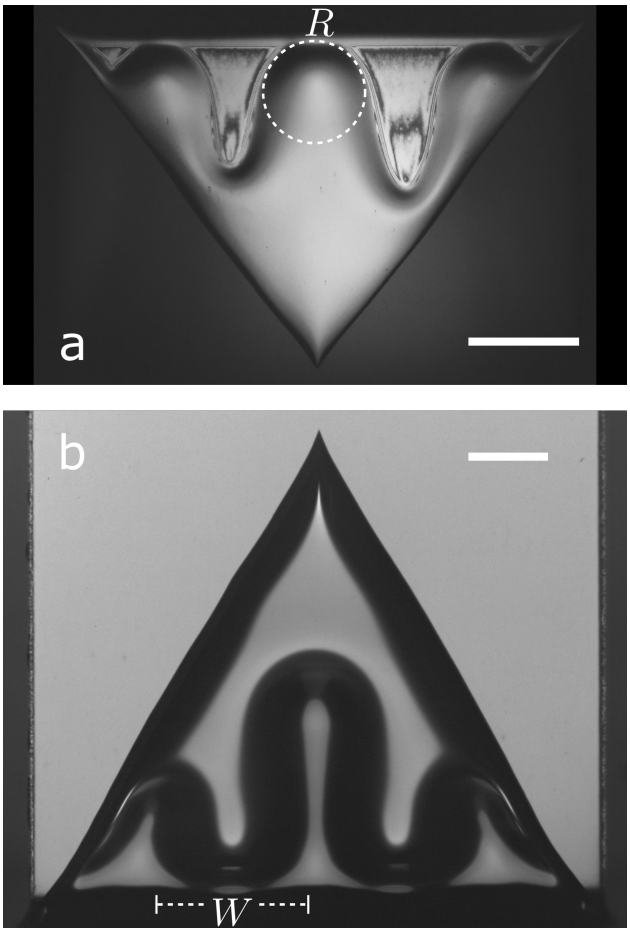

Figure 4.2: Increasing substrate width, w, increases the number of thin-thick alternations in film thickness. (a) A 25.4 mm wide recording tape entrains an air film with 3 thick sections. The upper portion of the thin-thick boundary can be approximated by a circle of radius R. (b) A 35.3 mm wide acrylic plate entrains a water-glycerin film with 2 thick sections with width W. In a and b the substrate widths, w, are approximately twice what they were in the corresponding images shown in Fig. 1.1a and b. Scale bar: 5mm.

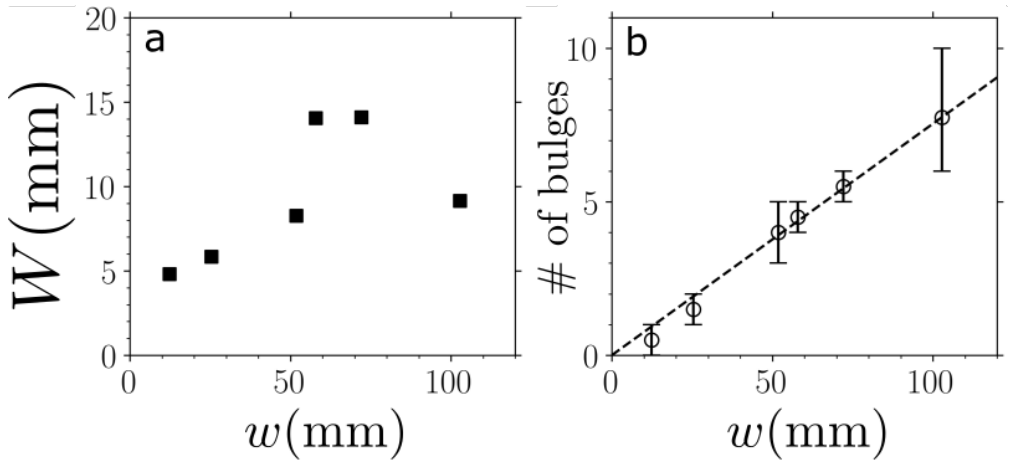

Figure 4.3: (a) Width of a thick section, W, versus substrate width, w, for water dewetting a mylar surface. (b) Number of thick parts, N, versus w, for water dewetting a mylar surface. Error bars indicate different thin-thick configurations observed, for a given w. Dashed line: linear fit to the mean observation.

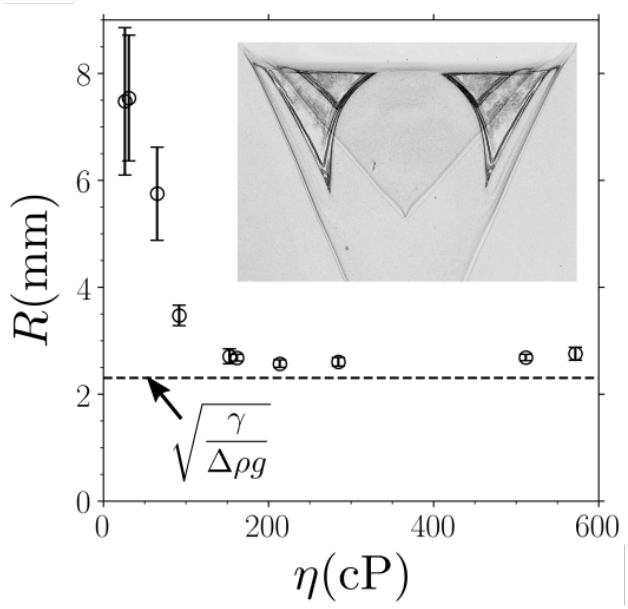

Figure 4.4: Radius of curvature, R, of the upper portion of the thick part, versus liquid viscosity, η for forced wetting. Dashed line: capillary length $l = \sqrt{\gamma/\Delta\rho g}$. Inset: superimposed edge-detected images of two different air films, entrained into different liquids of viscosities $\eta = 160$ cP & 290 cP respectively at $U = 150$mm/s.

buoyancy and interfacial tension. The inset of Fig. 4.4 shows the superimposed images of two air layers entrained in two different viscous liquids (both with $\eta > 90$cP). The two shapes have very different outlined V shapes, but the curves of the thin-thick boundary overlap very well.

4.2 Wetting velocity of the contact line

The upside-down V shape of the contact line was quantitatively interpreted by Blake and Ruschak in terms of the maximum velocity that a contact line could move across a substrate [1]. When the substrate velocity U exceeds the maximum value, $U_{\max}$, the stationary contact must become inclined by an angle ϕ so that the velocity of the contact line normal to its surface, U_n, does not exceed $U_{\max}$:

$$U_n = U\cos\phi \leq U_{\max}. \tag{4.1}$$

Figure 4.5a shows one example of the inclination angle of the lateral contact line, ϕ, tracked continuously from onset until it has reached its steady state value. Clearly ϕ, and therefore U_n from Eq. 4.1, does not remain constant during this time of gap formation; ϕ_{on} initially reaches a maximum, and decreases to a steady state value ϕ_{ss}. ϕ_{on} is consistently smaller than ϕ_{ss} for different viscosities and different tape velocities.

Figure 4.5b and c show $(\cos\phi)^{-1}$ versus U at onset and in the steady state respectively, for various liquid viscosities. From Eq. 4.1, the nearly linear relationship indicates a constant U_n. There exists a nearly constant U_n independent of U for each viscosity, but the value is different at onset from what it is in steady state. In the steady state, the curves depart significantly from linearity at larger velocities.

We fit our data to the relation $(\cos\phi)^{-1} = U_{n,\text{fit}}^{-1}U$ (Eq. 4.1) in each linear regime. The resulting $U_{n,\text{fit}}$ is shown in Fig. 4.5d, plotted versus η. The average normal velocity $U_{n,\text{fit}}$ is

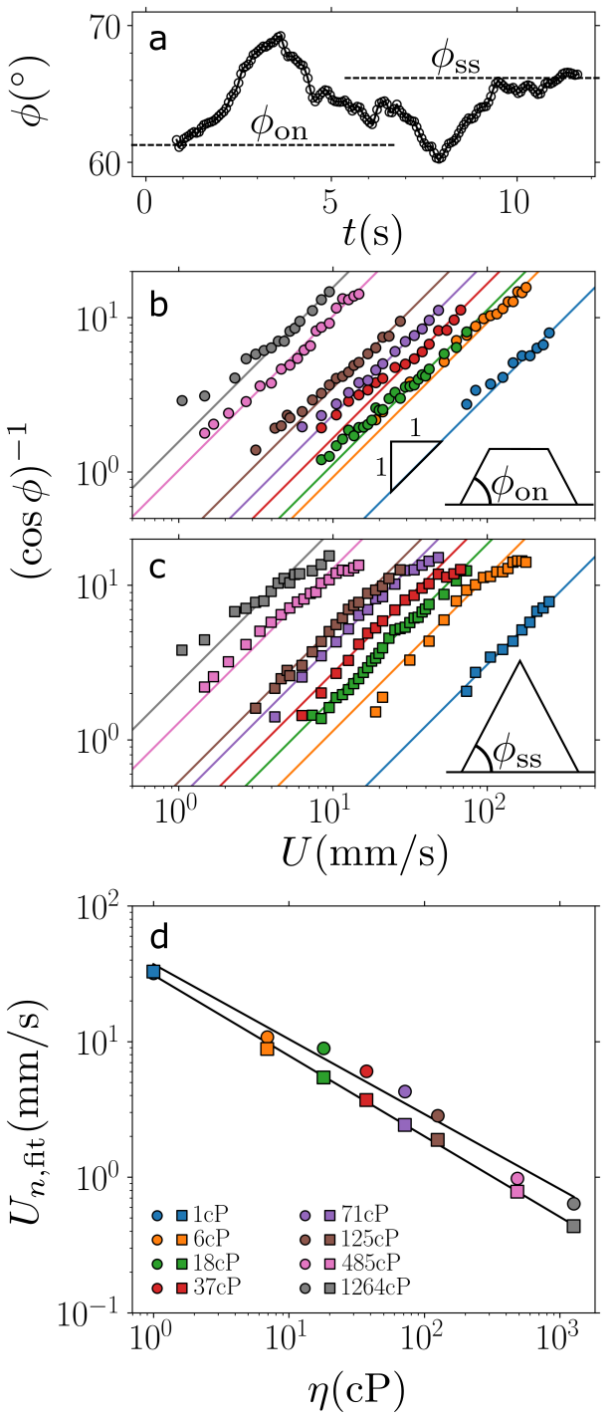

Figure 4.5: (a) Inclination ϕ of side contact line, versus time, t, during a typical contact-line evolution to a V-shaped steady state. ϕ_{on}: inclination angle at onset; ϕ_{ss}, inclination angle at steady state. (b) and (c) $(\cos\phi)^{-1}$ versus U for onset and steady state respectively. Solid lines: linear fits to each data set. (d) Fitted normal relative velocity, $U_{n,\mathrm{fit}}$, versus liquid viscosity η for both onset and steady state. Top solid line: $U_{n,\mathrm{fit}} \propto \eta^{-0.55}$. Bottom solid line: $U_{n,\mathrm{fit}} \propto \eta^{-0.59}$.

consistently larger at onset than it is in the steady state as was noted above from Fig. 4.5a.

A fit to the power law $U_{n,\text{fit}} \propto \eta^{\alpha}$ gives:

$$\alpha_{\text{on}} = -0.55 \pm 0.032 \tag{4.2}$$

$$\alpha_{\text{ss}} = -0.59 \pm 0.010. \tag{4.3}$$

We note the power laws hold for over 3 order of magnitude of viscosity. In contrast to previous two-dimensional lubrication analyses on a horizontal contact line [4, 15, 2], U_n is not inversely proportional to η.

For the case of steady-state forced wetting, our previous work [7] concluded a power law for the relation between the normal wetting velocity, U_n, versus the viscosity of the *outer* liquid, η_{out}, where an air pocket is entrained into:

$$U_n \propto {\eta_{\text{out}}}^{-0.75 \pm 0.03}. \tag{4.4}$$

Therefore, the normal relative velocity, U_n, decreases with increasing viscosity both in the case of the inner fluid (as in the case of dewetting) and for the outer fluid (as in wetting).

Kamal *et al.* [10] studied the contact line motion where the inner and outer fluids contribute nearly equally to the dynamics. This is the case for forced wetting near the contact line. Although air has a much smaller viscosity than the viscous liquid, the viscous dissipation cannot be neglected because of the sharp wedge near the contact line (see also [9, 13]). In their theoretical work they concluded:

$$U_n \propto \frac{\log \eta_{\text{out}}}{\eta_{\text{out}}}. \tag{4.5}$$

Figure 4.6 shows the extracted $U_{\max}$ from [7], versus $\log \eta_{\text{out}}/\eta_{\text{out}}$. The experimental data is fit very well by the Kamal analysis.

During the formation of the liquid pocket, I measure the relative normal velocity for the

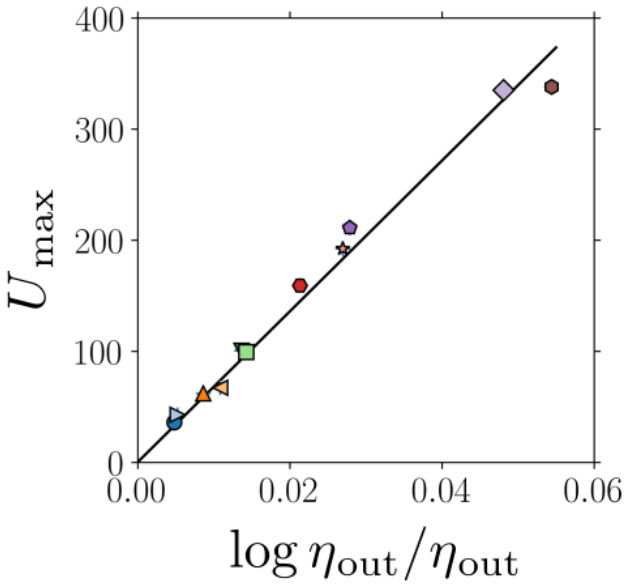

Figure 4.6: Maximum wetting velocity in forced wetting, $U_{\max}$, versus $\log \eta_{\text{out}}/\eta_{\text{out}}$. Solid line: least-square linear fit to data.

nearly horizontal section of the contact line by directly tracking its displacement over time. For a typical process, Fig. 4.7a shows the superimposed positions of the contact line at equal time intervals until the trapezoid has reached the triangular shape (as seen in the third panel of Fig. 4.1).

The normal component of the local relative velocity of the contact line can be calculated at each point (x, y):

$$U_n(x, y) = (U - U_{\text{cl}}(x, y)) \cos \varphi(x, y), \tag{4.6}$$

where φ is the *local* inclination of the contact line. In Fig. 4.7a, the calculated magnitude field $U_n(x, y)$ swept out by the nearly horizontal contact line during this period is mapped in the same figure to a color scale. The color map shows a significant decrease ($\sim 50\%$) in normal relative velocity, U_n, throughout the process.

Although along the entire contact line at a given instance there is a relatively consistent normal wetting speed U_n, the value of U_n changes over time so that the maximum wetting velocity, Eq. 4.1, is not constant throughout the creation of the wedge. The same conclusion

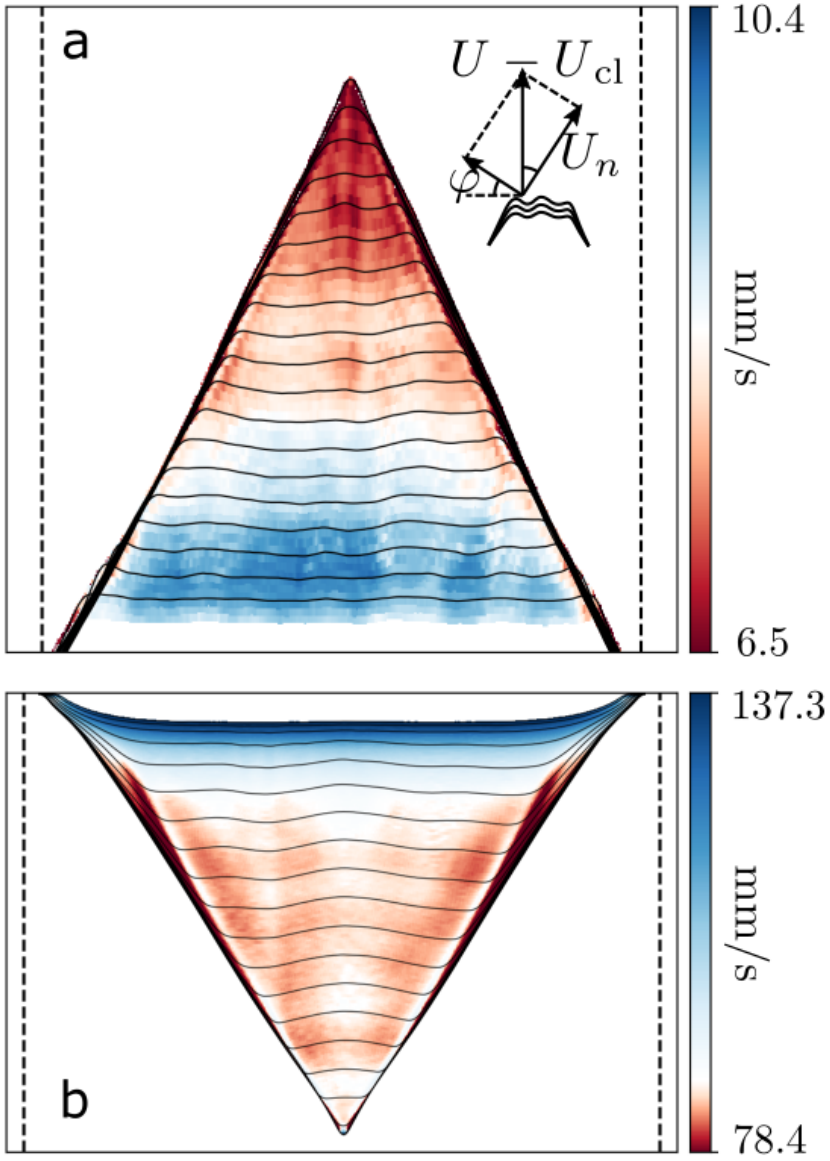

Figure 4.7: Normal relative velocity, U_n, of contact line during formation of a V. Color scale: U_n deduced from Eq. 4.6. (a) Contact-line positions at intervals of 100 ms, for an acrylic moving out of a water-glycerin mixture of viscosity $\eta = 18$ cP at $U = 15.8$ mm/s. (b) Contact-line positions at intervals of 50 ms, for a mylar moving into a water-glycerin mixture of $\eta = 226$ cP at $U = 130$ mm/s.

applies for the case of forced wetting, as shown in Fig. 4.7b.

4.3 Thickness structure of wetting layer

Figure 4.8 shows measurements of the thin and thick regions of the dewetting layer. The first row shows a measurement of the thin, flat part. In the image shown in the top left panel, the arrow and white spot indicate the position where the measurement is taken: near the bottom middle of the frame. The top middle panel shows the circular fringes from the high-speed camera (⑤ of Fig. 2.2). Using the maximum likelihood method described in the Methods Section allows clear identification of the interference rings; the top right panel shows the reconstructed pattern $X_0(x, y, \beta_{\text{optimal}})$. The height of the entrained layer in this region is $h_{\text{optimal}} = 84.2\mu m$. Similarly the second row shows a measurement of the thick part of the entrained fluid when it expands to touch the bottom with the focused beam placed near the bottom right as shown by the arrow. A thicker fluid layer gives rise to a much denser set of fringes, and the maximum likelihood fitting gives $h_{\text{optimal}} = 285.0\mu m$.

To see the influence on the steady-state thickness h, due to the substrate width w, I measured the thickness of both the thin and thick regions for various substrate widths, w. In Fig. 4.9, when w is varied, h of the thick region fluctuates, and does not show an apparent general trend. The thin part becomes slightly thicker ($\sim 20\%$) as the width, w, is increased by a factor of ~ 5.

For a fixed substrate width, w, Fig 4.10 shows measurements in the dewetting steady state of the thin and thick regions as a function of liquid viscosity η and substrate velocity U. As is shown for both regions, h, normalized by the capillary length $l = \sqrt{\gamma/\rho g}$, is approximately a power law in the capillary number: $Ca = \eta U/\gamma$:

$$h/l \propto Ca^{\alpha}. \tag{4.7}$$

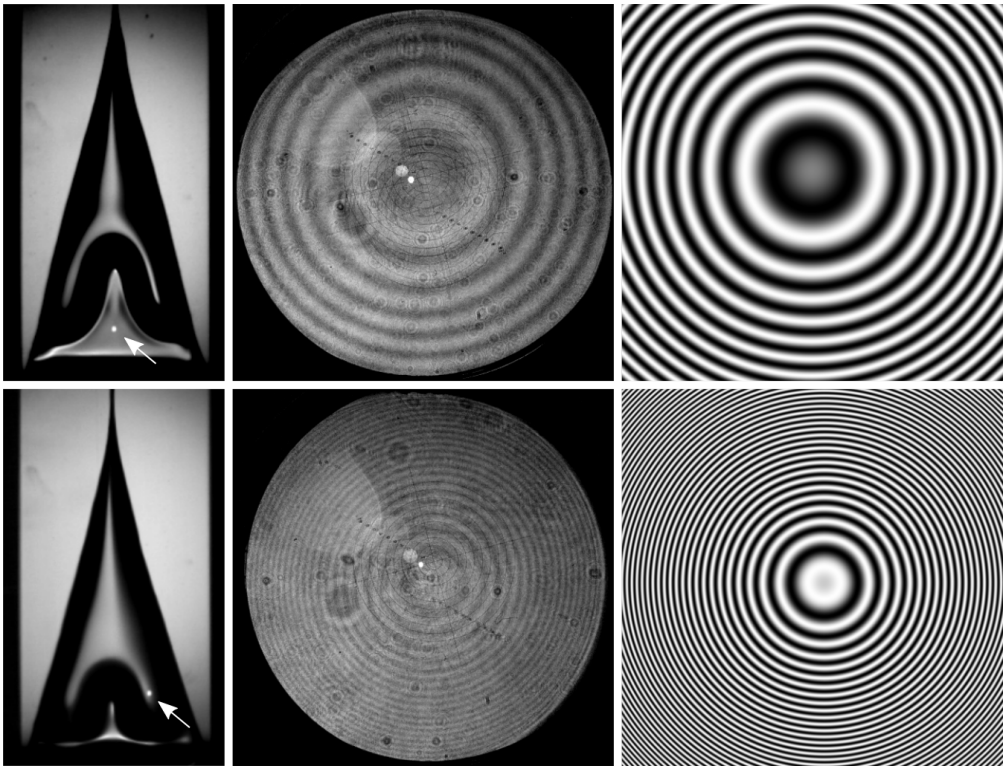

Figure 4.8: Thickness fitting by likelihood maximization. An acrylic substrate travels out of a liquid of viscosity $\eta = 18$ cP at $U = 17$ mm/s. Left column is an image of the entrained fluid. The arrows pointing to focusing spots indicate location of the measurement. Middle column: corresponding interference fringes captured by high-speed camera. Right column: reconstructions of fringes using maximizing likelihood, giving thicknesses of $h = 84.2$ μm for the thin region (top row) and 285.0 μm for the thick region (bottom row).

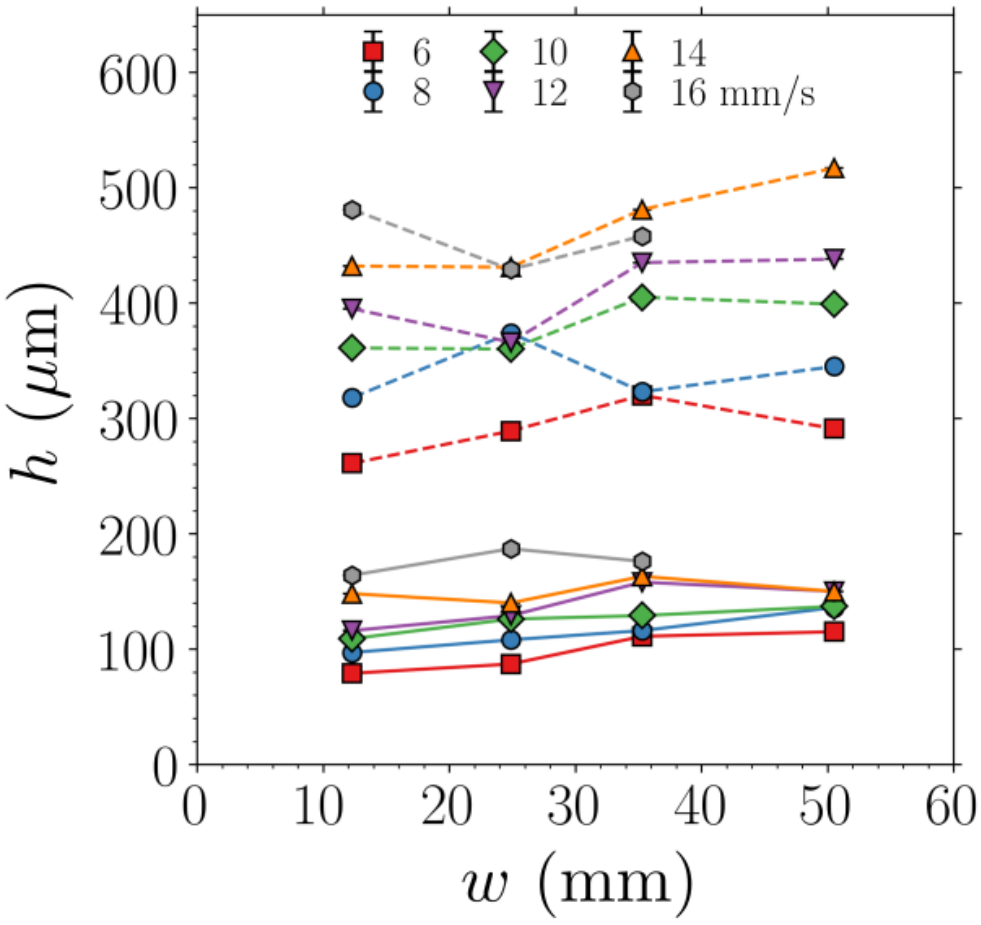

Figure 4.9: Thickness, h, versus substrate width, w, for steady state of dewetting. Markers connected by solid lines: thin part. Markers connected by dashed lines: thick part. Liquid viscosity $\eta = 41$ cP.

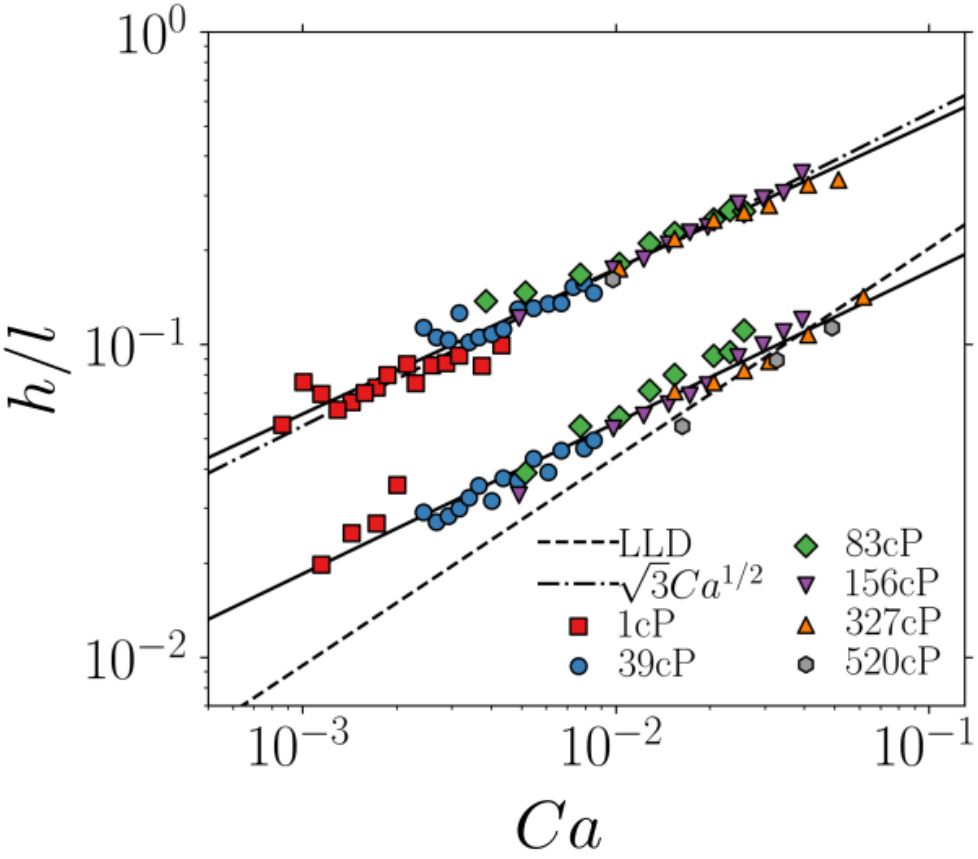

Figure 4.10: Thickness normalized by capillary length, h/l, versus capillary number Ca, in a log scale. Top solid line: $h/l \propto Ca^{0.46}$. Bottom solid line: $h/l \propto Ca^{0.48}$. Substrate width $w = 17.1$ mm

For over 2 orders of magnitude in Ca, I find

$$\alpha_{\text{thick}} = 0.46 \pm 0.012. \tag{4.8}$$

This result can be understood by a similar argument as was used for the reversed situation of wetting [7]. We simplify the complex-shape of the liquid layer as a simple wedge with an average wedge angle, Θ, where it meets the substrate. We use the result of Huh and Scriven [9] that the interface velocity U_I is proportional to the substrate velocity U:

$$U_I = \zeta\left(\frac{\eta_{\text{in}}}{\eta_{\text{out}}}, \Theta\right)U, \tag{4.9}$$

where η_{in} is the viscosity of the inner fluid (water-glycerin mixture in our case) and η_{out} is the viscosity of the outer fluid (air in our case). In the limit of large $\eta_{\text{in}}/\eta_{\text{out}}$ ($10^2 \sim 10^5$ in our case) and small Θ (< 90), it can be shown that the proportionality ζ is approximately a constant, nearly independent of $\eta_{\text{in}}/\eta_{\text{out}}$ and Θ. Using the measured static receding contact angle 63° as an approximation to the dynamic contact angle Θ, we get $\zeta = -0.55 \sim 0.56$. The negative sign indicates that the flow at the interface is in the opposite direction of the substrate motion, about half in magnitude. We argue that the thickness is selected by maximum stability of the layer, so that Eq.7 of [7] can be directly applied :

$$\begin{aligned} h_{\text{thick}} &= \left(2(1-\zeta)\frac{\eta_{\text{in}}}{\Delta\rho g}U\right)^{\frac{1}{2}} \\ &= \sqrt{3.1}lCa^{\frac{1}{2}}. \end{aligned} \tag{4.10}$$

Equation 4.10 is plotted in Fig. 4.10 as the dashed-dotted line. As with the case of forced wetting [7], the simple argument gives a reasonable fit to the data. A more rigorous derivation using lubrication theory given by Snoeijer *et al.* [2] gives a nearly identical result as Eq. 4.10, with a pre-factor equal to $\sqrt{3}$. We note that these two arguments are equivalent in our dewetting regime since both effectively applied the no-shear boundary condition at

the liquid-air interface with flux conservation.

For the thin part, over 2 orders of magnitude in Ca, Eq. 4.7 also provides a good fit with

$$\alpha_{\text{thin}} = 0.48 \pm 0.016. \tag{4.11}$$

Although the exponent of the power law is close to that of the thin parts in the case of forced wetting [7], we emphasize a key assumption of [7] does not apply here: in forced wetting, we approximated the interface velocity as uniform. The thin-thick alternation, which is a large ratio when calculated for the inner fluid (air), is only a small perturbation when it is thought of as a change to the shape of the bulk outer fluid (liquid). Since the outer fluid (liquid) is the dominant fluid except very close to the contact line, it is reasonable to assume that the interface velocity is predominantly affected by the outer fluid and is thus roughly uniform. By contrast, in the case of dewetting, the inner fluid (liquid) plays the dominant role everywhere. The prominent thin-thick structure deviates greatly from a thin wedge, making the assumption of a simple, uniform interface velocity invalid.

The thin part thickness also significantly differs from the Landau-Levich-Derjaguin theory (LLD) [11, 3], which has an exponent:

$$\alpha_{\text{LLD}} = \frac{2}{3}. \tag{4.12}$$

The LLD prediction is plotted in Fig. 4.10 as the dashed line. The measurements deviate from LLD theory especially at low Ca. In the LLD theory, gravity and viscous dissipation are balanced, and the thickness of an *infinite* liquid layer is uniquely determined by matching the meniscus shape near the bath. Assuming in our case a similar balance between gravity and viscous dissipation, the discrepancy suggests that our thin-part thickness h_{thin} is not selected by meniscus matching. The existence of the contact line and much thicker parts nearby, which is not incorporated in the LLD theory, presumably plays an important role. Further modelling is required to quantitatively interpret our result Eq. 4.11.

The method of maximum-likelihood fitting is also carried out for the case of wetting. Figure 4.11a shows a laser image of a part of the entrained air film. There are interference fringes which are noisy and have artifacts such as a dust shadow on the bottom left. The air film patch is divided into 4 smaller parts, each of which can be approximated by a parabolic shape. Our fit for individual parts give satisfactory results, as shown in the middle image. Notice the slight mismatch near the boundaries of adjacent parts. This indicates the inadequacy of the parabolic model near the edge (rather than the inadequacy of the algorithm). The right-most image shows a simple example of local edge detection for the same pattern, which in general cannot capture the features of main interest, and is not robust against errors. The reconstruction of the tomography of the air film is achieved by stitching these data patches together. The result is shown in Fig. 4.11b, with perspective views from two different angles.

4.4 Onset on a wide substrate: intermediate thickness

Numerous theoretical and experimental work (e.g. [16, 14, 15, 2, 12, 5]) focused on the thickness of a non-wetting liquid film during *onset*. They indicated that two different film thicknesses appear during the deposition: a leading thick film followed by a thin film that could be described by LLD theory. Using the interferometric method discussed above, I have also measured the film thickness during the onset and I plot this data in Fig. 4.12.

During the onset stage, there is a leading thick bulge near the contact line. When it expands and develops into a flat, thick film, the thickness, h_{thick}, is measured and can be fitted to $h_{\text{thick}}/l \propto Ca^{0.56\pm0.023}$ (top solid line). This differs from conclusions of previous analysis [16, 15, 14, 5], where h_{thick} is a function of the *relative* capillary number, Ca^*, which does not vary with Ca.

There is an extended thin region of thickness, h_{thin}, behind the leading thick film. It can be fitted to $h_{\text{thin}}/l \propto Ca^{0.55\pm0.018}$ (bottom solid line). This thin film is close to the LLD prediction $h_{\text{LLD}}/l = 0.946Ca^{2/3}$ (dashed-dotted line), confirming previous studies of

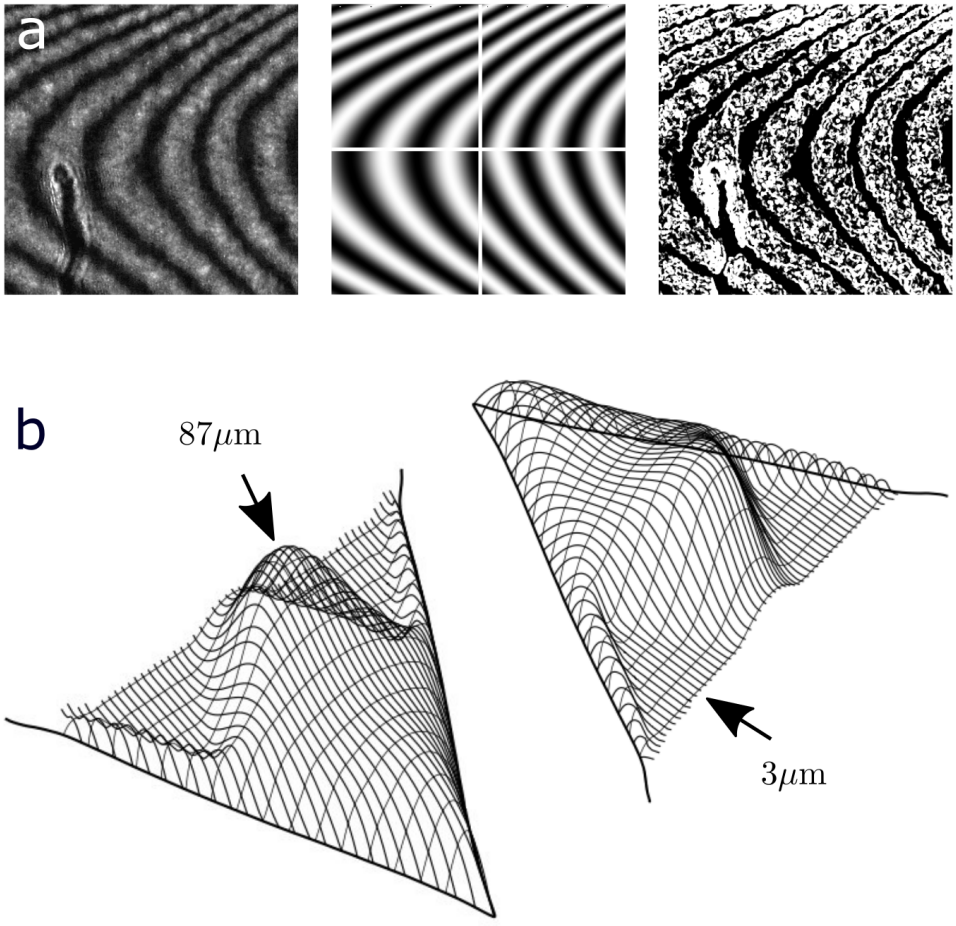

Figure 4.11: (a) Fringe fitting using likelihood maximization in forced wetting. Left: interference fringes of equal height produced by part of an air film. Middle: Fringes reconstructed by maximum likelihood fitting. Frame partitioned into 4 smaller parts for separate fitting. Right: a typical local edge detection algorithm for comparison. (b) Tomography of an air film reconstructed. Peak thickness: 87 μm; Thin flat part: 3 μm. Absolute thickness obtained by using multi-wavelength interference discussed in [7].

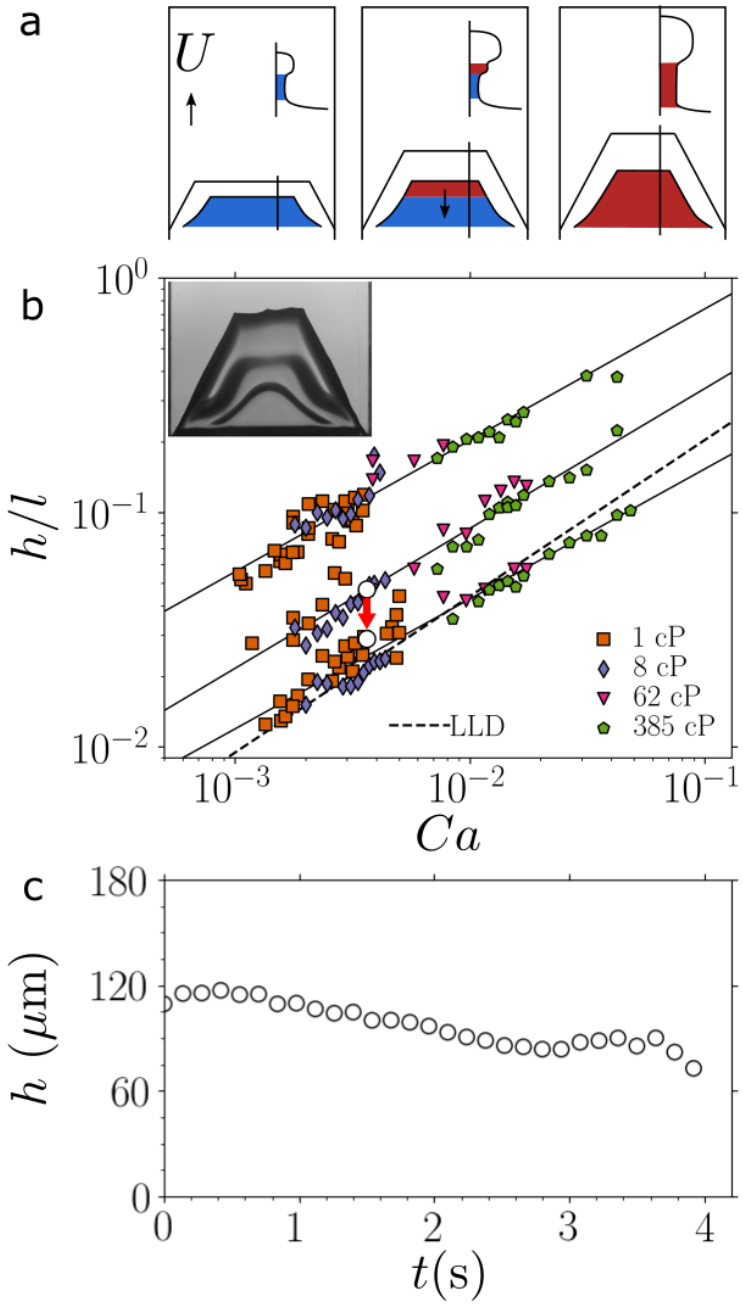

Figure 4.12: (a) Schematic showing the onset of an entrainment on a wide substrate. From left to right: behind a thick leading film near the contact line, a film (red) of intermediate thickness emerges to replace the thin film (blue). (b) Measured thickness scaled by capillary length, h/l, versus Ca. Top solid line: $h/l \propto Ca^{0.56}$. Middle solid line: $h/l \propto Ca^{0.60}$. Bottom solid line: $h/l \propto Ca^{0.55}$. Inset: typical image of onset film, showing the thick, intermediate, and thin regions. Substrate width $w = 37.7$ mm. White circles with an arrow: thickness range in (c). (c) Thickness change over time during onset for the film behind the thick region. Substrate width $w = 17.1$ mm.

the onset of the entrainment [14, 12, 5].

In addition, there appears a new region of intermediate thickness, which has not been reported in previous works. The thin film close to LLD prediction turns out to be transient. It is left behind immediately after the entrainment begins, only lasts a short period, and is rapidly replaced by a region of intermediate thickness h_{int} ($h_{\text{thin}} < h_{\text{int}} < h_{\text{thick}}$). The thickness change is discontinuous. This process is shown in the schematic drawing of Fig. 4.12a. The intermediate film can be fitted to $h_{\text{int}}/l \propto Ca^{0.60\pm0.021}$ (middle solid line). Numerically $h_{\text{int}} \approx 2h_{\text{thin}}$, over two decades of Ca range.

It is also observed that when the substrate width w is small, this phenomenon of discontinuous thickness change during the onset does not occur. The thinner film left behind by the leading thick film does not have a constant thickness over time, but instead decreases over time. In Fig. 4.12c I show a typical decrease of thickness. This decrease is also plotted in Fig. 4.12b as the white circles. As can be seen, with a narrow substrate the thickness of the entrained film behind a thick region changes continuously from near h_{int} to near h_{thin}, during the onset.

CHAPTER 5

CONCLUSION

I have presented an experimental study on various aspects of dewetting, and have systematically compared the results with those found in forced-wetting experiments. I have discovered a prominent structure in the layer of steady-state dewetting, consisting of well-defined thin-thick alternations transverse to the direction of substrate motion, behind a V-shaped contact line.

For both wetting and dewetting, I found quantitatively that the normal relative velocity is larger during the onset than it is at steady state. This is different from the previous simple model of a fixed maximum wetting speed.

To characterize and quantify precisely the thin-thick structure in the dewetting layer, I developed a method, combining interference information from varying the angle of incidence and data fitting with maximum likelihood. Power-law relationships are found between layer thickness h and capillary number Ca over two decades of Ca range, for different parts of steady state. The thickness of steady state thin part in dewetting differs from various existing models. The new pattern-fitting algorithm also helps to reconstruct the tomography of the air layer in forced wetting.

Lastly, onset of dewetting entrainment has been examined and I found a new region, whose thickness is in between two known regions predicted and observed in various previous studies.

This work shows that dynamic partial wetting is far more complex than accounted for in various simple models. Future work is needed to quantify and understand the contact-line velocity variation as well as the mechanism for thickness selection in the steady state. Further experiments on wetting in two-liquid systems, where both liquids contribute significantly, can help to examine and clarify the argument of stability.

REFERENCES

[1] TD Blake and KJ Ruschak. A maximum speed of wetting. *Nature*, 282(5738):489, 1979.

[2] Giles Delon, Marc Fermigier, Jacco H. Snoeijer, and Bruno Andreotti. Relaxation of a dewetting contact line. part 2. experiments. *Journal of Fluid Mechanics*, 604:55–75, 2008.

[3] BVCR Derjaguin. Thickness of liquid layer adhering to walls of vessels on their emptying and the theory of photo-and motion-picture film coating. In *CR (Dokl.) Acad. Sci. URSS*, volume 39, pages 13–16, 1943.

[4] Jens Eggers. Hydrodynamic theory of forced dewetting. *Phys. Rev. Lett.*, 93:094502, Aug 2004.

[5] Peng Gao, Lei Li, James J. Feng, Hang Ding, and Xi-Yun Lu. Film deposition and transition on a partially wetting plate in dip coating. *Journal of Fluid Mechanics*, 791:358–383, 2016.

[6] Nathan Gold, David L Willenborg, Jon Opsal, and Allan Rosencwaig. Method and apparatus for measuring thickness of thin films, March 12 1991. US Patent 4,999,014.

[7] Mengfei He and Sidney R. Nagel. Characteristic interfacial structure behind a rapidly moving contact line. *Phys. Rev. Lett.*, 122:018001, Jan 2019.

[8] LF Hoyt. New table of the refractive index of pure glycerol at 20 c. *Industrial & Engineering Chemistry*, 26(3):329–332, 1934.

[9] Chun Huh and L.E Scriven. Hydrodynamic model of steady movement of a solid/liquid/fluid contact line. *Journal of Colloid and Interface Science*, 35(1):85 – 101, 1971.

[10] Catherine Kamal, James E. Sprittles, Jacco H. Snoeijer, and Jens Eggers. Dynamic drying transition via free-surface cusps. *Journal of Fluid Mechanics*, 858:760–786, 2019.

[11] L. D. Landau and B. V. Levich. Dragging of a liquid by a moving plate. *Acta Physicochimica URSS*, 17, 1942.

[12] M. Maleki, M. Reyssat, F. Restagno, D. Quéré, and C. Clanet. Landau–levich menisci. *Journal of Colloid and Interface Science*, 354(1):359 – 363, 2011.

[13] Antonin Marchand, Tak Shing Chan, Jacco H. Snoeijer, and Bruno Andreotti. Air entrainment by contact lines of a solid plate plunged into a viscous fluid. *Phys. Rev. Lett.*, 108:204501, May 2012.

[14] J. H. Snoeijer, J. Ziegler, B. Andreotti, M. Fermigier, and J. Eggers. Thick films of viscous fluid coating a plate withdrawn from a liquid reservoir. *Phys. Rev. Lett.*, 100:244502, Jun 2008.

[15] Jacco H. Snoeijer, Bruno Andreotti, Giles Delon, and Marc Fermigier. Relaxation of a dewetting contact line. part 1. a full-scale hydrodynamic calculation. *Journal of Fluid Mechanics*, 579:63–83, 2007.

[16] Jacco H. Snoeijer, Giles Delon, Marc Fermigier, and Bruno Andreotti. Avoided critical behavior in dynamically forced wetting. *Phys. Rev. Lett.*, 96:174504, May 2006.

[17] Soap, Detergent Association, et al. Glycerine: an overview. *Terms, Technical Data, Properties, Performance*, 1990.

[18] Koichi Takamura, Herbert Fischer, and Norman R. Morrow. Physical properties of aqueous glycerol solutions. *Journal of Petroleum Science and Engineering*, 98-99:50 – 60, 2012.